

Comparison of full-scale rockfall tests with 3D complex-shaped discrete element simulations

B. Garcia ^{a,b,*}, P. Villard ^a, V. Richefeu ^a, D. Daudon ^a

^a Laboratoire 3SR, University of Grenoble Alpes, CNRS, Grenoble INP, Grenoble, France

^b IMSRN-GINGER, Ingénierie des Mouvements de Sol et Risques Naturels, 680 Rue Aristides Bergès, 38330 Montbonnot, France



ARTICLE INFO

Keywords:

Rockfall
Real-scale tests
Discrete elements method
Shape effect
Hard and soft grounds

ABSTRACT

Trajectory analysis is often needed to handle rockfall hazards. It is crucial to understand and to refine ground and rock interactions during a rockfall, which can be related to the elements involved. They include the topology, ground and rock nature, but also the volume and shape of the falling blocks. This work focuses on replicating field observations using a 3D discrete elements model (DEM) in order to further analyze the possible rockfall deposition areas, which may not be accessible due to the limited number of experimental data available. The numerical model implements blocks of more realistic shapes that were reconstructed from in situ blocks obtained by photogrammetry. The dissipation of kinetic energy at the collision point is suitably managed. In the experimental campaign, dozens of boulders (rock block) releases were conducted on two slope profiles of a quarry located in Authume (France). Block passing heights, velocities and runout distances were assessed at specific ground points. We analyzed lateral spreads, propagation distances, and energy balances computed for 3 different block geometries. These numerical results were confronted with experimental observations. Although time-consuming compared to lumped mass and rigid body dynamics models where the impact duration is zero, the DEM used in this work is versatile thanks to an explicit consideration of geometrical effects throughout the life of multiple contacts. It allows to simulate quite accurately a multitude of configurations. Among the properties of the terrain and the blocks, geometric features are shown to be crucial. For the sake of efficiency, a simplified shape coefficient based on block's elongation is proposed.

1. Introduction

In geotechnical practice, the use and tryout of state-of-the-art numerical methods is a common procedure when the engineer seeks to obtain the optimal, most reliable and best supported result, especially in structure design. The engineer's practice is not restricted to a single choice, and to fulfill customer's requirements, there are many trajectory analysis codes capable of satisfying different needs.

In order to identify probable deposition zones for risk estimation, engineering offices make use of numerical tools that integrate empirical methods, such as the *Shadow Cone* or the *Energy line* method (Jaboyedoff and Labroue, 2011; Heim, 1932; Hungr and Evans, 1988). Although successful in many situations, such strategies can only be applied under specific circumstances, where the topography does not present abrupt variations in the profile studied, which may result from pre-existing earthworks (e.g., embankments) or valley slope-lines. While empirical methods are widely used, many valuable features of the trajectory of a

boulder cannot be examined, for instance, energy losses and passage heights at selected locations in the path of a detached block. Such datasets are essential, as they are the basic inputs for the design of protective works. Empirical methods are, in fact, used for large-scale cases to assess hazards and define the most likely pathways. Previously recorded field observations in the deposition areas are also of great value. Trajectory analysis codes become then necessary to refine structure designs, but also for improving the hazard zoning.

According to a recent report of the European inter-regional project *RockTheAlps* (Kobal and Zabota, 2018), empirical methods represented, in 2018, only 15% of the methods used for the study of gravitational movements, against 59% of studies based on trajectory analysis models (so called trajectography). This balance reflects the strong interest of the community to increasingly use trajectory analysis in their studies.

Thus, the study of boulder trajectory highlights the need to refine the understanding of the phenomena involved in rockfalls and interactions with the ground, according to the nature of all the elements in play.

* Corresponding author at: Laboratoire 3SR, University of Grenoble Alpes, CNRS, Grenoble INP, Grenoble, France.
E-mail address: bsgarcia18@gmail.com (B. Garcia).

Based on the equations of motion (principle of body dynamics), the more detailed description of each phase of the rock block trajectory involves both software development and a sound knowledge of basic mechanics. Trajectory analysis approaches can be classified in a number of ways, and this categorization is becoming less obvious as the approaches become more sophisticated. A first classification can be made according to *spatiality*, i.e. the way in which the movement of projectiles is dealt with in space. The codes can therefore be classified into: 2D (propagation occurs over a vertical plane), 2.5D (or “pseudo-3D”, taking into account elevation), and 3D (when surface meshes are reconstructed using lasergrammetry or photogrammetry techniques). In a global way, the codes simulate, for many initial conditions, the trajectory of a single block, for which the free flight phase obeys the classical Newton’s law of motion under gravity acceleration.

Several trajectory analysis models have been developed since the 70s, the same moment when discrete elements code (Cundall and Strack, 1979) first appeared to solve specific geotechnical problems. They were based on lumped mass or rigid body approaches and often restricted to two dimensions – e.g., Rocfall (Rocscience), CRSP (Colorado Rockfall Simulation Program), PROPAG-CETE Lyon (Rochet, 1987), PFC (ITASCA). Great improvement was observed from 90’s, as computational power evolved and more powerful machines became popular. Since then, 3D methods started to emerge such as RocPro3D (Cottaz et al., 2010), Yade (Kozicki and Donze, 2008), RAMMS (Bartelt et al., 2018), PFC-3D (ITASCA) as well as hybrid approaches like HY-STONE (Valagussa et al., 2014) and stochastic/process-based ones like Rock-yfor3D (Dorren, 2016). Numerical approaches used on trajectory analysis codes are listed in detail in the relatively recent work of Dorren et al. (2006); Leine et al., 2014; Volkwein et al., 2011.

Although there are several sophisticated tools on the market, it remains difficult to assess the relevance and consistency of the results obtained from such codes, either because of a lack of in-depth understanding of the role of the parameters or physical laws used in the code, or because of the lack or incompleteness of the recommendation guides that can vary from a country to another. It must be said that this fact does not result from a lack of effort on the part of research laboratories and the developers themselves, who in fact invest time and energy in understanding and applying the tools to real case studies (see, e.g., the recent paper by Bourrier and Acary (2022)). The implementation of realistic block shapes adds an extra complexity to perform 3D parameter calibrations.

2. Context

The present numerical study deals with real scale experimental data obtained in the framework of the C2ROP French National Project (Rockfall Hazard, Risk and Protective structures), with which we aimed to identify and assess the rock shape effects on the runout distances and the propagation paths by using a 3D discrete elements model (3D-DEM) developed in Laboratoire 3SR (Richefeu and Villard, 2016). Compared to other methods, the use of 3D-DEM, although time-consuming during the calculation phases and for the definition of input data, brings physics and richness to numerical simulations. A great interest in studying collisions using numerical methods of this type is to find correlations and thresholds that can feed stochastic models. In particular, taking into account the real shape of the blocks gives a better objectivity to the obtained results.

The national C2ROP project was motivated by the need of sharing new methods and tools that are constantly being developed to enhance rockfall hazard assessment; particularly those designed by research groups and by private sector industry. As part of this project, an experimental rockfall campaign (managed by INRAE in October 2017) was conducted to assess variabilities in rockfall kinematics and stopping positions (Bourrier et al., 2020). Such experiments are complex to carry out and require specific means adapted to data recording. Full-scale rockfall experiments have been performed in the past and are

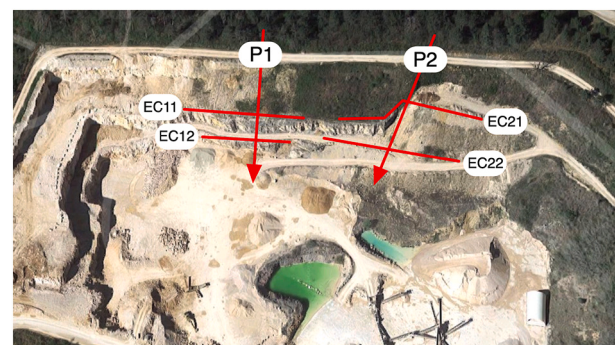


Fig. 1. Aerial view of the Authume quarry, showing the two profiles P1 and P2, and the virtual barriers EC11, EC12, EC21, and EC22 (image from Google Earth).

available upon request; some of these were performed by private companies. Other rockfall tests can be found in the works of the following authors (Bourrier et al., 2012; Bartelt et al., 2018; Pichler et al., 2005; Bar et al., 2016).

The site selected by the national project C2ROP consortium¹ is the Authume quarry, located at Dôle, in the Jura department (France). This quarry is 300 m wide and up to 70 m long (Fig. 1). Bedrock consists of pink Callovian limestone. The topological properties do not really correspond to a natural slope since the terrain is modified by mining exploration. However, this site was chosen among others by the national C2ROP project partners through a joint selection process, particularly for its ease of access and for its topography with vertical cliff walls, rocky and vegetated slopes, and flat areas that suggest the most likely propagation corridors. Fig. 1 shows the configuration of Authume site and the two launching profiles: P1 and P2. The virtual barriers EC11 to EC22 are established to determine the velocities and heights of passage at these specific points for each of the propagation path.

A total of 89 blocks of different sizes and shapes were released during the experimental campaign (41 blocks on profile P1 and 48 on profile P2). To test the ability of the numerical tool to simulate such events, we compared the experimental and numerical data, such as the velocities at each of the virtual barriers. This allows for a better analysis of the energies lost from the launch point to their stop location in the quarry. The contact parameters for the discrete model were determined on the basis of field observations and *in situ* tests performed in an engineering context. Different shapes and sizes of virtual blocks were considered in order to define the sensitivity of these parameters on the propagation distances, energies, and velocities at different points of the propagation path.

3. Discrete element procedures

3.1. Overview, novelties, and methodology

The discrete element tool used for this work is a 3D application developed by Richefeu and Villard (2016); among other features, it allows to analyze the trajectory of isolated blocks up to their stop, or of rocky mass of small volume (in the order of 1000 m³) in interaction with a slope. Its specificity lies in its ability to simulate complex physic behaviors such as energy dissipation mechanisms at the particle scale and to take into account realistic geometries for blocks and slopes. This approach, which explicitly takes into account the distinct aspect of the blocks, employs 3 parameters to handle the dissipation phenomena at each collision point: in the normal, tangential, and also spinning directions. The main interest of the collision force law proposed (see Section 3.3) is that it guarantees a controlled energy dissipation ratio for

¹ Chute de blocs rocheux, risques, ouvrages de protection: www.c2rop.fr

each collision, with no particular assumption about the physical mechanisms involved, which implies that the evolution of the force during the contact is in reality only a technical means for satisfying this need. The addition of spheropolyhedral shapes (Section 3.2) has made it possible to model the geometry of rock blocks in a more realistic way. Topographic roughness can also be taken into account while maintaining the three dimensions, which adds complexity and refines the analyses that are now numerous and richer in detail. The mesh dependency on the interaction models leads us to propose weighing solutions for multiple forces that are balanced for the same collision (Garcia, 2019).

In the simulations, the blocks were released without initial velocity from the four corners of a square area ($4\text{ m} \times 4\text{ m}$) for each of the two profiles. Both launching zones with their four release points are shown in Fig. 2. These starting points were the same regardless of the shape of the simulated block. In terms of initial orientations, the numerical simulations were performed by successively rotating the block by an angle of 45 degrees with respect to each of the three main axes. In total, a number of $4^3 = 64$ orientations for 4 release points were used, which corresponds to $4 \times 64 = 256$ simulations per studied shape.

3.2. Block geometries

The shape of the rigid bodies is modeled by *spheropolyhedra* (SP). This approach makes it possible to reproduce realistic block shapes that are as complex as necessary. They can be concave and even have recessed parts, which is not allowed with most other approaches to model polyhedral shapes – generally limited to convex geometries. In addition, the definition of a shape can be built from a photogrammetric survey or a lidar. Fig. 3(left) shows the SP model of a stone reconstructed by photogrammetry technique.

From a strictly mathematical point of view, a SP can be considered as the Minkowski sum of a polyhedron and a sphere (Richefeu and Villard, 2016). Another way to define a SP is to think of it as a polyhedron with rounded corners. The set of possible contact configurations between two SP can be managed from four elementary configurations depending on the interacting elements forming the spheropolyhedra: vertex-vertex, vertex-edge, vertex-face, and edge-edge. Fig. 3(right) outlines these configurations. Note, though, that the face-to-face configuration is not one of the elementary configurations. The determination of the mass properties of each SP is detailed in Richefeu and Villard (2016) and Garcia (2019). In our in-house computational tool, a variety of techniques borrowed from the world of video games is used, because the problems we deal with are in fact very similar. The use of a physics engine library – like bullet (Coulmans and Bai, 2016–2021) – makes sense, and would certainly lead to very improved computation times. However, this kind of library does not handle a multitude of contact points between pairs of polyhedra, and this feature is crucial in the proposed model.

Three characteristic dimensions of the blocks, taken from the photographs, were defined as the lengths L_1 , L_2 , and L_3 of the best-fitted

bounding box; Fig. 3(left)). This box can be defined as the smallest parallelepipedic volume that completely encloses the block. For volume estimation, this box does not give helpful hints because global irregularities, like angularity, are not taken into account. However, they provide the minimal information needed to apply most of the shape classification methods based on the three main dimensions, such as the classifications of Sneed and Folk (1958); Zingg, 1935; Erdogan et al., 2006; Williams, 1965. These latter methods were applied for the collected dataset and analyzed in detail in Garcia (2019).

In this study, in order to evaluate the effect of shape in terms of trajectory and stopping of the blocks, a simplified shape coefficient has been introduced. It allows the recognition of two main types of geometries: compact and elongated shapes. This geometrical criterion is very similar to the one proposed by Erdogan et al. (2006) who differentiated two main types: platy and elongated. Its main drawback is that there are many undetermined cases, especially those for which the ratio L_1/L_2 is much higher than 1 and the ratio L_2/L_3 different from 1. This limitation induces the operator to define a threshold that separates platy from elongated shapes. The proposed shape criterion is based on a quantity, the elongation coefficient s_c , defined by considering the main dimensions of the best-fitted bounding box (L_1 , L_2 , and L_3 , such that $L_1 > L_2 > L_3$) by:

$$s_c = \frac{L_1}{L_2} - 1 \quad (1)$$

In this relation, it is estimated that, for a block to be said compact in shape, its longest length L_1 must not exceed its intermediate length L_2 by more than 30%. Otherwise, i.e. when $s_c > 0.3$, the block is said elongated. As most blocks exhibit a L_2/L_3 ratio close to 1 (Bourrier et al., 2020), the threshold value of 0.3 is chosen in agreement with visual observations in the field.

To perform a back analysis of the block launching experiment, we intended to reconstruct the block shapes using photogrammetry. Due to difficult exposure conditions right after the experimental campaign – such as direct exposure to sunlight, many dark areas, and limited time – it was not possible to systematically reconstruct all the blocks that were released. Nevertheless, realistic block shapes were obtained, prior to the experimental campaign, during a field trip; Fig. 4. The SP3A shape was generated from the block shot of launch number 89; it is, therefore, the only reconstructed geometry of an actually launched block.

Block SP1A has a volume three times smaller than the one of block SP2A. The elongation coefficient of block SP1A ($s_c = 0.27$) is close to that of block SP2A ($s_c = 0.22$), which means that this latter is, according to the proposed classification, slightly more compact than block SP1A. We can nevertheless consider these two shapes as enclosable by a cube (see Table 1).

In the following sections, block SP1A is referred to as the “small cubic block”, and block SP1B is said “medium cubic block”. Block SP2B, labeled “large cubic block”, has a volume similar to the volume of the largest block released in the experimental campaign. As said before,

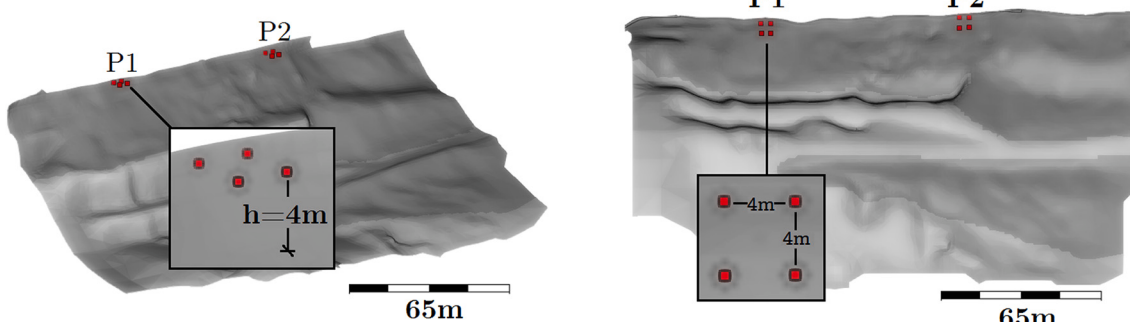


Fig. 2. Release points of profiles P1 and P2 displayed on the triangulated mesh used for the numerical simulations.

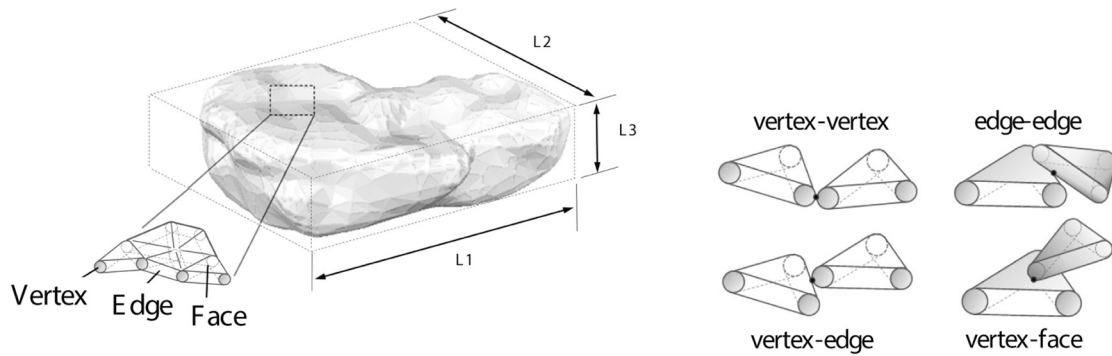


Fig. 3. (Left) Sphero-polyhedral (SP) geometric model of a pebble mesh reconstructed using photogrammetry and triangular tessellation. Concretely, a sphero-polyhedra is a rigid assembly of 3 elementary shapes: spheres for the vertexes, tubes for the edges, and polygons for the faces. (Right) Sketch of the four elementary configurations for any multiple contact configuration between two sphero-polyhedra.

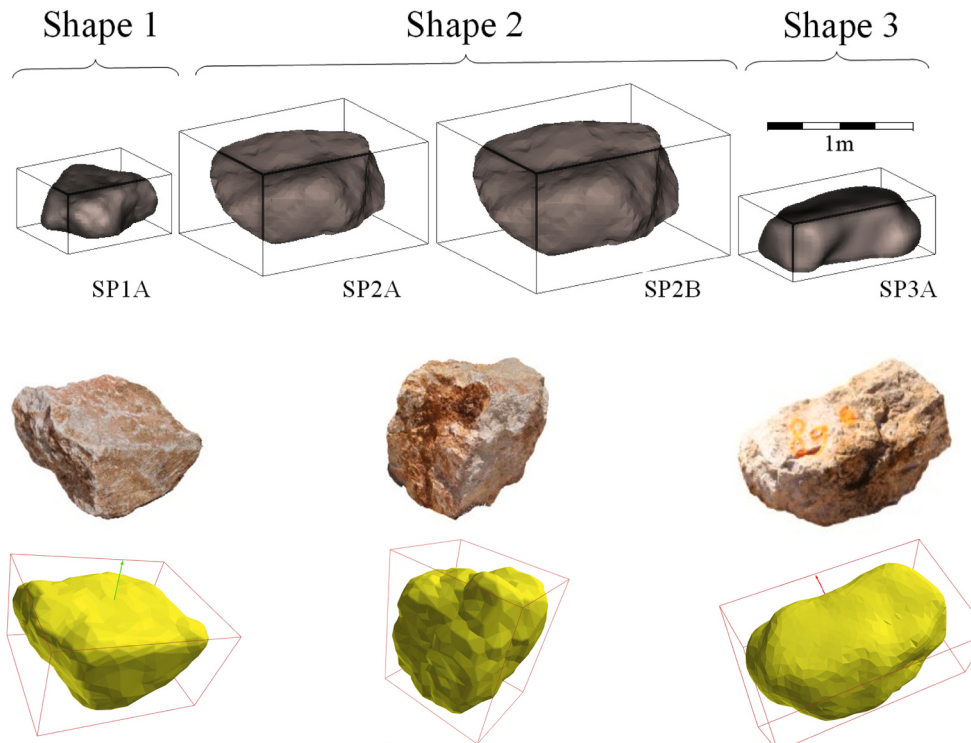


Fig. 4. (Top line) shapes of blocks reconstructed by photogrammetry; (Middle line) photographs of the corresponding blocks taken on the site; (Bottom line) reconstructed shapes rounded with a small radius as used by the DEM code Rockable. The SP1A shape is the smallest. The SP2A and SP2B shapes are identical but with different volumes. The SP3A shape is the only one that was experimentally released; it is also the most elongated ($s_c = 0.74$).

Table 1
Characteristics of the blocks used in the simulations.

Block shape label	Volume (m ³)	Mass (kg)	I_x (kg·m ²)	I_y (kg·m ²)	I_z (kg·m ²)	s_c (-)
SP1A	0.137	343.5	12.27	20.29	16.40	0.27
SP2A	0.589	1472.5	141.87	228.65	176.74	0.22
SP2B	0.707	1767.5	191.27	317.42	240.40	0.22
SP3A	0.205	514.0	48.75	55.75	18.40	0.74

block SP2B is homothetic of block SP2A by a factor of 120%. This allowed us to study the effect of the volume increase on the propagation while keeping the same geometry. Block SP3A ($s_c = 0.74$), which is the only one belonging to the experimental campaign, was denoted as “small elongated block”.

In the dataset, we looked for flattened blocks. According to the classification by [Sneed and Folk \(1958\)](#) shown in Fig. 5, we however realize that most of the blocks released are of a compact nature (>60%). The classification of the three shapes used in the simulations on this ternary system is marked by cross symbols in Fig. 5(a). Blocks SP1A, SP2A and SP2B are classified as *Compact Bladed* and SP3A as *Bladed*. Thus, it is noticed that the simulations with only “blade-shaped” blocks are justified by their shape classification, which is rather close to that of the experimental blocks. The coefficient s_c seems to operate well for this dataset; this is certainly due to the number of flattened blocks being too few to perform a meaningful statistical analysis (only one block is classified as platy in the whole dataset). Therefore, it is important to be aware that, in the case of a study carried out on a terrain of exfoliated rock for example, the shape coefficient s_c will have to be reconsidered or adapted because it does not really address the block platyness.

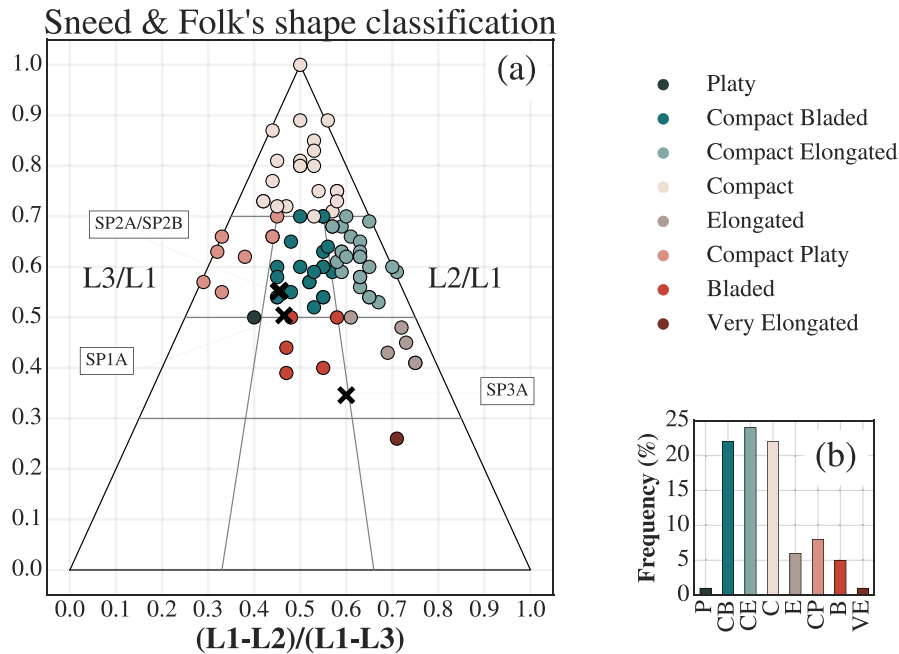


Fig. 5. Three-pole classification according to Sneed and Folk (1958): (a) Circle markers are experimental data, cross markers denote block shapes used in the simulations of this work; and (b) Frequency of launched block shapes according to their location in the three-pole classification. Adapted from Bourrier et al. (2020).

3.3. Collision law

Simple, although effective, linear elastic laws are used, allowing dissipation of kinematic energy in the normal, tangential, and radial directions (Richefeu and Villard, 2016). The associated elastic stiffnesses are, respectively, k_n , k_t , and k_r . The normal force is updated at each explicit time step δt with a model that can be summarized as follows:

$$f_n(t + \delta t) = \begin{cases} f_n(t) - k_n \dot{h}_n(t) \delta t & \text{if } \dot{h}_n \geq 0 \quad (\text{loading}) \\ -k_n e_n^2 h_n(t) & \text{if } \dot{h}_n < 0 \quad (\text{unloading}) \end{cases} \quad (2)$$

where e_n^2 is the rate of energy restitution in the contact normal direction, $\dot{h}_n(t)$ is the block velocity normal to the ground at time t , and $h_n(t)$ is the penetration distance of the block. The force is calculated incrementally under charge (as long as the block sinks into the ground), and directly under discharge (from the moment the block starts to leave the ground).

This implies a force jump that will have no repercussion on the global calculation in the context of repeated “round trip” collisions in rockfall problems. On the contrary, the energy balance is finely controlled through the parameter e_n^2 without any assumption on the physical mode of dissipation over the time scale of a whole collision (load followed by unload). Fig. 6(a) illustrates the evolution of the normal force f_n during a collision as a function of the penetration h_n of the block inside the ground at a contact point. The shaded area represents the energy lost in this case, and it can be shown that the rate of lost energy is $1 - e_n^2$ for a round trip collision.

The energy restitution rate e_n^2 can be figured out from the rebound of block mass m falling vertically on a surface, without tangential or rotational velocity. In this situation, the post-collision energy relative to the pre-collision energy is written as follows:

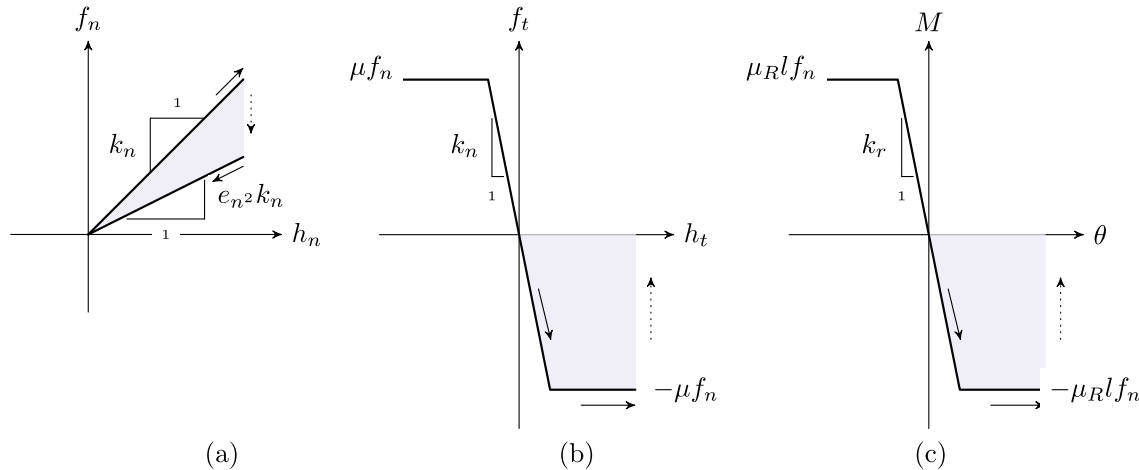


Fig. 6. Collision laws for: (a) the normal force f_n , (b) the tangential resistant force f_t , and (c) the moment at constant f_n . The respective stiffnesses k_n , k_t , k_r , and the dissipation parameters e_n^2 , μ and μ_R are represented therein. Shaded areas represent the dissipated energies (remaining work of force or moment for a round trip collision).

$$\frac{\frac{1}{2}mv_{y+}^2}{\frac{1}{2}mv_{y-}^2} = \left(\frac{-v_{y+}}{v_{y-}} \right)^2 = (e_n)^2 \quad (3)$$

The tangent force f_t is updated at each time step with the following increment:

$$\Delta f_t = \begin{cases} -k_t \dot{h}_t(t) \delta t & \text{if } |f_t| < \mu f_n \\ 0 & \text{otherwise} \end{cases} \quad (4)$$

where \dot{h}_t is the relative sliding velocity, and the dissipation parameter μ incorporates both friction and abutment. Each increment of tangent forces $k_t \dot{h}_t \delta t$ acts in the opposite direction to the slip. The parameter μ can reflect all the mechanisms involved in a collision as long as the resulting loss of kinetic energy is in the same direction as the slip (Richefeu and Villard, 2016). Fig. 6(b) gives an illustration of the tangent force law in the particular situation where the normal force is assumed constant. This is a very unlikely situation for collision events, but the purpose is just to explain how the model works. Shaded areas represent the energy that would be lost if the contact were suddenly lost. We see, in this usual case for an impact, that the elastic energy is not restored. This undesirable effect can be made imperceptible by using a sufficiently high tangential stiffness k_t .

The moment of resistance M is calculated using a very similar way to the tangent force (Eq. (4)). It is called rolling friction. The purpose is to account for the action of soft ground (humpy or indented ones) which could decrease the block's rotation. It is updated at each time step with the following increment:

$$\Delta M = \begin{cases} -k_r \dot{\theta}(t) \delta t & \text{if } |M| < \mu_R \ell f_n \\ 0 & \text{otherwise} \end{cases} \quad (5)$$

These parameters can be deduced from an optimization procedure described in detail in Garcia (2019), which was applied to the experimental campaign of this study.

The use of (sphero-) polyhedral shapes, regardless of the technical solution chosen, presents certain complications that are not generally addressed in the literature. The concern is that many contact possibilities exist when two bodies collide with each other, especially when a fine mesh is used. As a result, the apparent stiffness becomes proportional to the number of contact points, which depends on the positioning of the bodies and the geometric algorithm used for collision detection. Therefore, if nothing is done, the stiffness involved cannot be kept constant as the number of contact points evolves uncontrollably. The problem is even more intricate than it seems. Here are some supporting arguments:

- It may be argued that the apparent stiffness of the soil is related to the area of contact with the impacting block, but the number of contact points is not necessarily related to the extent of this area (the mesh may be degraded/simplified or not);
- It is possible to obtain, especially with concave surfaces, multiple contact points which are independent, whereas in the situation of a contact between two plane faces, these points are geometrically (and artificially) identified and have in fact nothing to do with the small contact zones which would result from non-regular surface states;
- Thus, mesh resolution is a parameter that affects apparent stiffness.

It is essentially this last point that prompted us to propose a tricky solution to overcome this artifact. To control the apparent stiffness k_n between two sphero-polyhedra i and j (the reasoning is valid for k_t or k_r), a weight is applied to the stiffness of the underlying contact points $N_c^{ij}(t)$, at each time t , by a weight w^{ij} such that:

$$\sum_{N_c^{ij}(t)} w^{ij}(t) = 1 \quad (6)$$

The solutions and physical arguments to define the values of the

weights are multiple. The choices proposed and implemented in the code solve some of the inconveniences, but not all of them. In particular, the fine transmission of the elastic forces may be biased, but fortunately, the elastic response is of secondary importance in the rockfall situations treated in this work.

One of the solutions can be a amount-based weighing, which consists in distributing the weights equally as it follows:

$$w^{ij}(t) = \frac{1}{N_c^{ij}(t)} \quad (7)$$

Another strategy, based on overlaps, is to assign greater stiffness to those contacts less subject to normal deflection:

$$w^{ij}(t) = \frac{h_n^{ij}(t)}{\sum h_n^{ij}(t)} \quad (8)$$

where $h_n^{ij}(t)$ is the local deflection at a point of contact between bodies i and j .

In both proposed solutions, the weights are the same regardless of the local loading direction (normal, tangential, and rotational). In the present work, the weighing solution based on contact deflections (Eq. (8)) has been employed for all discrete simulations. Some justifications for this choice can be found in Garcia (2019).

3.4. Digital terrain model and zoning of ground properties

A raster map and a cloud of points with an accuracy of 0.2 m were provided as an input of the benchmark. The model is defined by GPS coordinates (x, y , and z) which served as the basis for the terrain surface reconstruction. The cloud of points was then transformed into a triangular mesh (TIN format), and the resolution has been lowered to 0.5 meters (see Fig. 7). This meshed surface, transformed into a sphero-polyhedron by the addition of a sweeping sphere, constitutes the digital terrain model (DTM).

As a DTM is composed of triangles, spheres, and cylinders just like rock blocks, the problem of multiple contacts also arises for the block-terrain interactions. The ability of the DEM to incorporate finite interaction durations, with contacts that can be multiple, is a key element of the modeling. It allows geometric inputs to be expressed during the interactions of a block with the terrain, which is not the case with the usual methods (lumped mass or rigid body dynamics) where each contact involves a unique interaction without duration. The zoning consists in defining different zones for which the nature of the rebounds or the energy dissipation mechanisms are characterized by their own properties. An analysis based on on-site investigations required a lot of expertise and feedback to obtain a representative zoning of the studied site. In the Authume quarry, 3 main zones can be distinguished (see Fig. 7): the rocky parts for the vertical walls and the horizontal surfaces (grey zone), the rocky slopes (red zone) and the vegetated slopes (green zones). The dissipation parameters were determined following the optimisation method described in Garcia et al. (2017); Garcia, 2019. To this end, preliminary drop tests using small rocks were carried out on each type of bedding, which made it possible to establish an initial series of suitable and consistent parameters (Table 2).

4. Field results for comparison with simulations

The results presented in this section were provided by the campaign organization team (as part of the C2ROP project). They mainly concern the geometry of the blocks, the deposition zones, and the passing probabilities/velocities in the vicinity of virtual barriers.

4.1. Block characteristics and experimental procedure

A total of 89 blocks of different sizes and shapes were launched

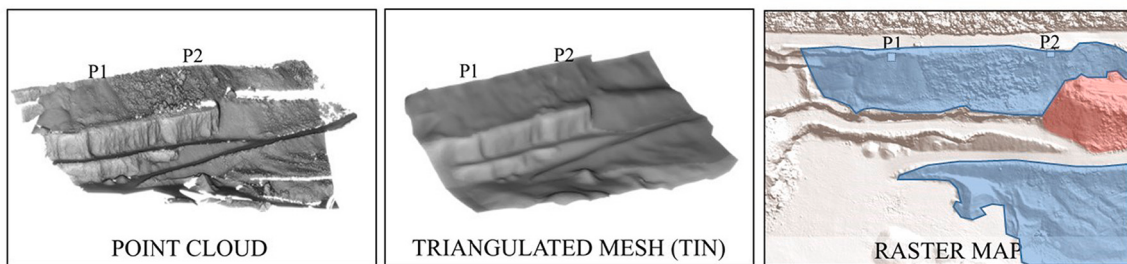


Fig. 7. Definition of the digital terrain of a part of the quarry. Cloud of 18 million points provided by the C2ROP organization. It was used to construct the triangular mesh (TIN) with a resolution of 0.5 meters. A raster map with a resolution of 0.2 m was also provided.

Table 2
Dissipation parameters for each zone.

	e_n^2	μ	μ_R
Red zone	0.01	0.70	0.18
Blue zones	0.01	0.70	0.35
Gray zone	0.01	0.30	0.00

during the experimental campaign (41 blocks on profile P1 and 48 blocks on profile P2). They were released by a mechanical shovel without initial speed at a height of about 1 m from the drop zone (about 4 m × 4 m in size). Following their fall and stop, the blocks were weighed and photographed under several viewpoints in order to reconstruct their geometry by photogrammetry. Thus their approximate size and volume could be estimated (recall here that the reconstruction was not perfect because of poor shooting conditions). The statistical distributions (percentages) of the mass of the blocks for profiles P1 and P2 are presented in Fig. 8.

The range and mean values of the block masses are summarized in Table 3 for each of the profiles and for both combined. We notice that the mass distribution of the blocks is far from uniform; a part of the blocks tested on profile P1 have a mass of the order of half a tonne (1 000 kg), and another part of the blocks have a mass approaching a single tonne. For Profile 2, we can notice an almost normal distribution with a peak of approximately 600 kg. Only 20% of the blocks (18 of the 89 blocks) have a mass greater than 1000 kg. Considering the shape criterion defined previously, 48.3% of the experimentally tested blocks can be qualified as elongated, and the remaining 51.7% have a so-called compact shape.

4.2. Deposition zones

The stop positions of the 89 released blocks are shown for the two propagation profiles P1 and P2 in Fig. 9. In this figure, different characteristic deposition zones can be distinguished and the percentage of blocks that pass through the virtual barriers (EC11, EC12, EC21, and

Table 3
Average, maximum, and minimum weight of the launched blocks during the C2ROP's experimental campaign.

Profile	Average weight (kg)	Maximum weight (kg)	Minimum weight (kg)
P1	806	1751	178
P2	706	1869	169
P1 & P2	752	1869	169

EC22) can be deduced. To simplify the reporting of the results, the deposits for profiles P1 and P2 have been respectively named A and B.

For both profiles, the percentage of blocks in the deposition zones A and B are given in Table 4. In profile P1, the spreading is characterised by:

- **Deposit 1A.** A single block that stopped near the release point.
- **Deposit 2A.** A single block that stopped at the top of the first rock face.
- **Deposit 3A.** 20 blocks that stopped between the virtual barriers EC11 and EC12.
- **Deposit 4A.** 19 blocks that stopped at the bottom of the second rock section.

In profile P2, the spreading is as follows:

- **Deposit 1B.** 4 blocks that stopped upstream the EC21 barrier. Three of these blocks deviated to the right, avoiding the slope corridor, and got stuck at the top.
- **Deposit 2B.** 3 blocks that crossed the EC21 barrier, went down the slope, and landed on the first track (excavation stair).
- **Deposit 3B.** 32 blocks that passed through the EC22 barrier and ended up on the second track (traffic path). Two blocks deviated very strongly along the sloping path towards profile P1.
- **Deposit 4B.** 8 blocks that passed through the EC22 barrier and stopped beyond the second track.

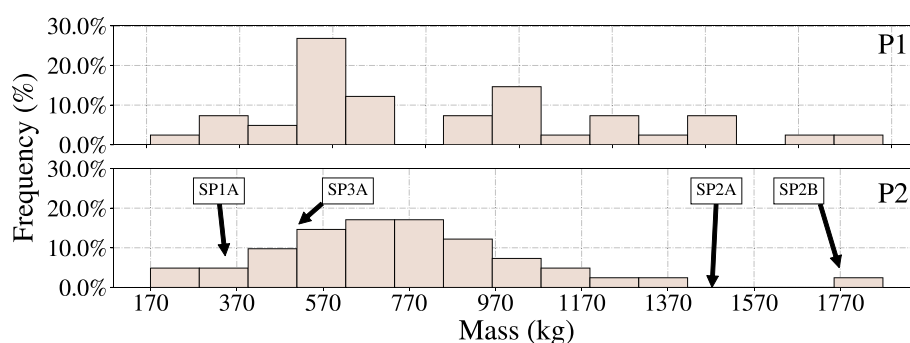


Fig. 8. Frequency of the number of blocks as a function of their mass (kg) for the profiles P1 and P2. The masses of the virtual blocks are also indicated on the histogram of profile P2.

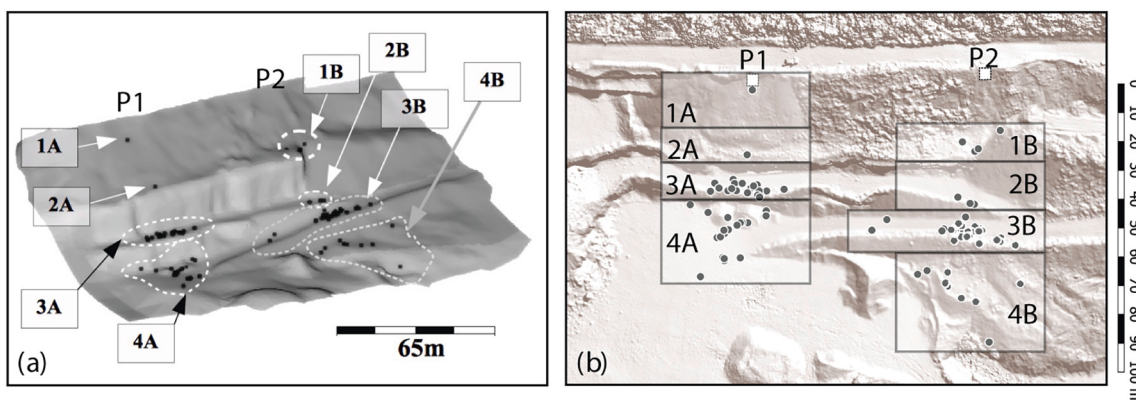


Fig. 9. Stop positions of the 89 released blocks (deposition zones) over the DTM used for the simulations. The deposits are referred to as A for profile P1, and B for profile P2. (a) 3D view adapted from Garcia (2019), Bourrier et al. (2020), (b) Top view of the stop positions.

Table 4

Percentage (and number) of blocks on deposits A and B for a total of 89 blocks (41 blocks for Profile P1 and 47 for Profile P2).

Deposit	A	B
1	2.44% (1)	8.51% (4)
2	2.44% (1)	6.38% (3)
3	48.78% (20)	68.09% (32)
4	46.34% (19)	17.02% (8)

Table 6

Rotational velocities in revolutions per second: collected experimental data.

Profile	P1	P1	P2	P2
Virtual barrier	EC11	EC12	EC21	EC22
Passing probability (%)	95.8	39.6	92.9	82.1
Average (rps)	1.43	1.27	1.67	1.79
Median (rps)	1.49	1.30	1.67	1.71
Standard deviation (rps)	0.38	0.39	0.52	0.55

5. Simulation results

The simulations of block propagation that will be presented below were performed using some experimentally collected data. They include the initial triggering conditions, the geometry and nature of the ground, the size and shape of the blocks, and their initial drop height. The influence of the shape and size of the blocks on the spatial distribution of the stop positions (along the mean steepest direction X and laterally) will be analyzed in this section. Propagation distances and velocities at the virtual barriers have been examined for the four numerical block geometries. Despite the fact that numerical blocks are not representative of the whole released blocks, a comparison with experimental data was also made.

The results presented for each block shape correspond to a total of 256 simulations (4 release positions multiplied by 64 block orientations). Nothing was specifically done to speed up the calculations as this was not the purpose of the study. It takes about half a day of computing to run each block release on a desktop computer (Intel® Xeon® W-2133 CPU @3.60 GHz). To achieve a series of 64 releases, one to two weeks of computation are required on a single workstation depending on the number of cores used and the resolution of the block. A number of optimizations are under consideration, but it is clear that in any case these times are far longer than those obtained with the usual methods based on a zero collision time. This is the price to pay for addressing shape effects in the interaction interactions.

5.1. Small cubic block (SP1A)

Block SP1A is the smallest digital boulder. Its volume is representative of a small part of the blocks launched during the experimental campaign. The stop positions of this block are shown in Fig. 11. Average passing heights and velocities are given for each virtual barrier in Appendix A. For profile P1, Fig. 11 highlights that the block stopped before a distance of $X = 25$ m (location of the virtual barrier EC11) for most of the release conditions. However, the maximum runout distance is 75 m. The prime deposition distance for profile P1 is located between 15 m and 20 m, and that of profile P2 extends from 40 m to 56 m, in a relatively

4.3. Passing probabilities and velocities at the virtual barriers

Translation and rotation velocities at virtual barriers (EC11, EC12, EC21, and EC22) are presented as average, median, standard deviation, and 95% percentile values, respectively in Tables 5 and 6. It can be seen that the mean values of the translation velocities vary, in relation to the barriers, from 1.9 m/s to 13.2 m/s with larger standard deviations for profile P1. These values are much higher in comparison to profile P2. Meanwhile, the rotation velocities of the blocks (given in revolutions per second, rps) are quite similar from one barrier to another and from one profile to another (average value around 1.6 rps). The standard deviations are also quite small.

Fig. 10(top) shows the distribution of translational velocities across the virtual barriers as a cumulative distribution function (CDF). Fig. 10 (bottom) is similar but it relates to rotation velocities. It can be pointed out that, for profile P1, more than 50% of the blocks passing through the barrier EC11 have translation velocities varying from 0 to 2 m/s; and the blocks passing the barrier EC12 have higher translation velocities (> 18 m/s). Indeed, blocks tend to gain energy due to free fall: 68% of them reach velocities ranging from 18 m/s to 19.5 m/s. At deposit 3A, only 32% of the blocks were moving at less than 5 m/s. In profile P2, the velocity distribution is rather symmetrical, with the exclusion of some blocks with very low velocities (< 2.5 m/s). Further discussions based on these CDFs and other details are available in Bourrier et al. (2020).

Table 5

Translation velocities in meters per second: collected experimental data.

Profile	P1	P1	P2	P2
Virtual barrier	EC11	EC12	EC21	EC22
Passing probability (%)	95.8	39.6	92.9	82.1
Average (m/s)	1.9	13.2	7.9	4.2
Median (m/s)	1.1	18.6	8.1	3.1
95% percentile (m/s)	6.8	19.2	11.2	8.8
Standard deviation (m/s)	8.5	8.5	2.2	3

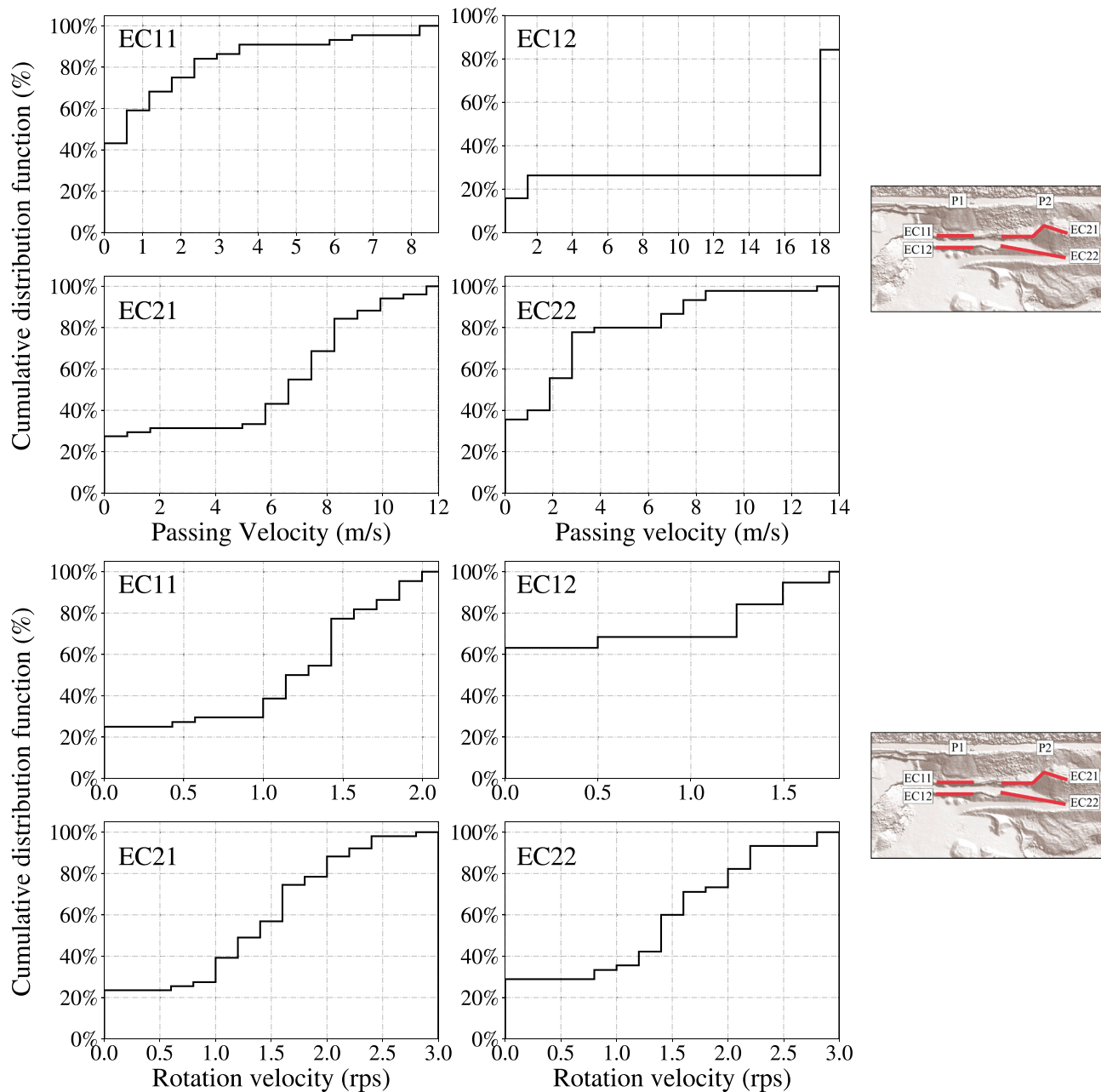


Fig. 10. (Top) Cumulative distribution function (CDF) of passing velocities (in meters per second) at virtual barriers EC11 and EC12 (Profile P1), and at virtual barriers EC21 and EC22 (profile P2). (Bottom) CDF of passing rotation velocity (given in revolutions per second, rps) at the same virtual barriers. Adapted from Bourrier et al. (2020).

uniform manner (compared to the deposit of the medium cubic block SP2A). The maximum runout distance for profile P2 is 70 m (20 m less than for the medium cubic block SP2A). There is a slight size effect causing the larger blocks (at similar density) to go further. We can notice that a large part of the blocks crossing the barrier EC22 settles on the intermediate flat ground, which is consistent with field observations.

The average value of the passage velocities through the EC11 barrier for block SP1A are rather close to those encountered experimentally for blocks of comparable size and shape: 2.64 m/s (see Appendix A.1(a)) against 1.9 m/s in the simulations. The average rotation velocity is 0.42 rps in the simulations, while this value was observed at 1.43 rps in the field. These features are similar to those found for the SP2A block. Numerically, the 95% percentile translation velocity is 4.68 m/s compared to 6.8 m/s on site, the average translation velocity through the barrier EC12 is 5.26 m/s (measured at 13.2 m/s on site), and the

average rotation velocity is 0.84 rps (measured at 1.27 rps on site). The value of the translation velocity for the 95% percentile is 7.37 m/s (Appendix A.2(a)), whereas for the experimental results, this value is 19.2 m/s. This difference is probably related to the fact that most of the blocks dropped experimentally are much heavier than the digital block SP1A. Only 5 blocks have a mass of less than 500 kg (Fig. 8). However, these facts also influence the statistics. We notice that between the EC11 and EC12 barriers, the blocks gain in energy (about a factor of 3 between the two barriers). For profile P2, we note (see Appendices A.3(b) and A.4(b)) a deceleration of the small blocks in translation (average passing velocities equals to 6.41 m/s through EC21 and to 4.83 m/s through EC22; velocities of the percentile at 95% of 8.48 m/s for EC21 and of 7.76 m/s for EC22). Rotation velocities also seem to decrease between the two barriers, both for the mean values and for the 95% percentile values (11.2 m/s for EC21 versus 8.8 m/s for EC22).

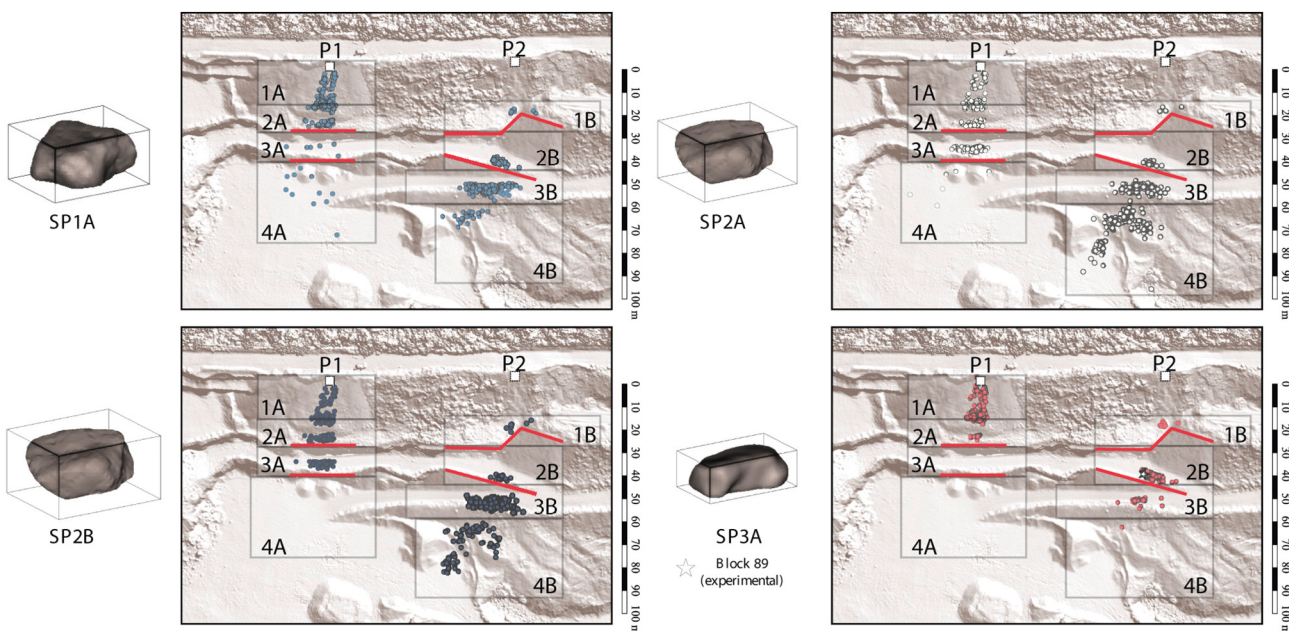


Fig. 11. Top view of the stop positions for the blocks SP1A, SP2A, SP2B, and SP3A. The star symbol shows real block 89 release end point (having the exact same shape as SP3A).

5.2. Medium cubic block (SP2A)

In general, the simulations (Fig. 11) reproduce fairly well the marked effect of slope and back-slope topography on the deposit zones, just as in the experimental tests. For profile P1, the maximum horizontal propagation distance reached by block SP2A is 58.5 m. There is little lateral dispersion in the launching zone. But as soon as the blocks cross the barrier EC11, the lateral dispersion increases. The geometry of the final deposit of the blocks is relatively conical when viewed from above. In profile P2, this effect is even more pronounced, but the general tendency is for the blocks to deviate more towards profile P1 (to the left). The blocks face greater 3D effects on this profile, which is more heterogeneous and irregular. The blocks go further (96.9 m) in profile P2, and this trend also corresponds to field observations. The deposits achieved by the simulations confirm a preferential stopping zone, related to the topography, for both profile P1 (from $X = 40$ m) and profile P2 (from $X = 50$ m). This also confirmed that the two profiles are topographically quite different since the blocks stop much further in profile P2.

Statistics generated for passing velocities and energies as well as passing heights at the virtual barriers EC11, EC12, EC21, and EC22 are synthesised, for comparison with the other block shapes, in the Appendices A.1(b), A.2(b), A.3(b) and A.4(b). For the EC11 barrier, the experimental value of average translation velocity is equal to 1.9 m/s with a standard deviation of 8.5 m/s (Table 5). With the simulations, this average amounted to 3.62 m/s with a standard deviation of 1.35 m/s. The numerical value of the 95% percentile (5.57 m/s) seems to be quite close to the experimental values (6.8 m/s, see Table 5). The average passage rotation velocity through the EC11 barrier is experimentally 1.43 rps (Table 6), to be compared to 0.58 rps for simulations. At the EC12 barrier, the mean value of the experimental translation velocity is 13.2 m/s (against 12.55 m/s for the numerical simulations) and the mean value of the experimental rotation velocity is 1.49 rps (against 2 rps for the simulations). Except for the results of the experimental mean velocities at the EC11 barrier, the numerical results seem to be in good agreement with the experimental measurements for profile P1. In the field it can be observed that most of the blocks crossing the EC11 barrier accelerate down the slope. The blocks mostly stop on the first platform and do not cross the EC12 barrier. The blocks that cross the platform have, on average, a higher velocity than the blocks that cross the EC11

barrier. The ratio of the average passage velocities between the EC12 and EC11 barriers is about 7 in the experiments, and 4 for the numerical simulations. The difference between the experimental and numerical values decreases when the percentile value at 95% is considered: the ratio becomes 3 for the experiments against 4 for the simulations. The total passage energies for the simulations increase from 25.68 kJ for the EC11 barrier to 262.50 kJ for the EC12 barrier. This corresponds to an increase in the average energy of the block by a factor of 10 between the barriers EC11 and EC12 related to the potential energy acquired by the block falling from a height of about 20 m.

For profile P2, Appendix A.3(b) presents the statistics of block SP2A as it passes through the virtual barrier EC21. The experimental average passage velocity is 7.9 m/s (6.74 m/s in simulations) and rotation velocities of 1.79 rps (0.69 rps in simulations). The experimental and numerical values of the 95% percentile also converge: 11.2 m/s (experiments) against 9.08 m/s (simulations). During the passage of the blocks through the virtual barrier EC22, we notice that the experimental results show a global tendency to a loss of energy in translation. The average experimental velocity of passage through the EC22 barrier is 4.2 m/s compared to 6.27 m/s numerically. However, relatively close values for the 95% percentile were obtained: 8.8 m/s experimentally versus 9.21 m/s numerically. The simulations indicate, in terms of average and 95% percentile of energy, a gain of two in rotational energy when passing the EC22 barrier (5.41 kJ) compared to passing the EC21 barrier (2.40 kJ).

5.3. Large cubic block (SP2B)

The volume of block SP2B corresponds to largest block launched during the experimental campaign. The shape of this block is the same as the one of block SP2A. In this way, it is possible to study the effect of the volume increase on the propagation, while keeping the same geometry. This comparative analysis will be made in more detail in the section dedicated to the study of the block geometry. Altogether, the results of block SP2B (Fig. 11) are, although different, broadly similar to those obtained with block SP2A. In profile P1, we can see that no block is deposited at the bottom of the slope. Three denser deposition zones can be distinguished: the first extends from 16 m to 24 m, the second is located between 26 m and 32 m, and the third lies between 36 m and 40

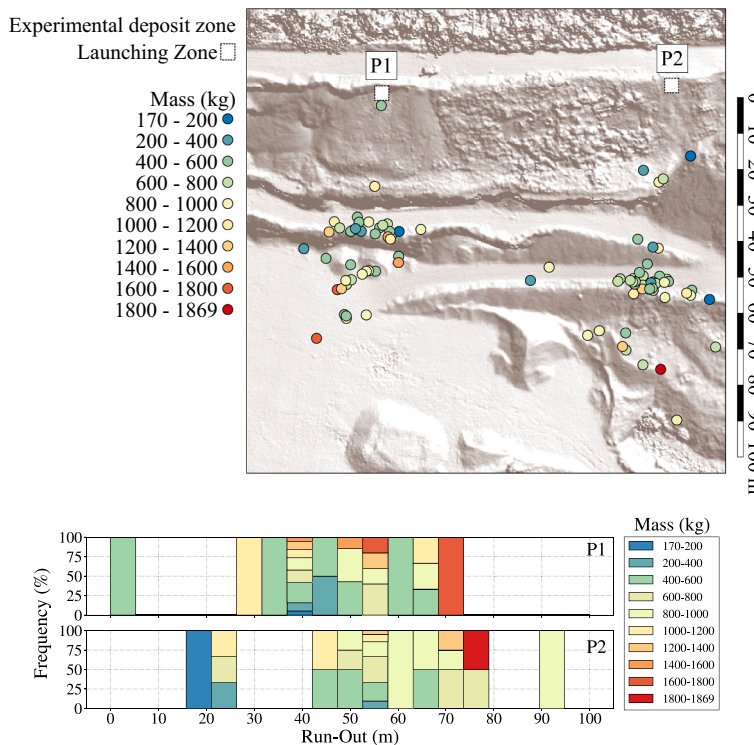


Fig. 12. Experimental stop positions in relation to the mass (kg). Heavier blocks go further on both propagation profiles.

m (after the EC12 barrier positioned at ~ 35 m). The maximum runout distance for this profile P1 is 40 m. In profile P2, most of the runout distances are comprised in the range from 55 m to 65 m (with a maximum of 87.6 m).

Passing energies for the block shape SP2B are globally higher than those of SP2A blocks, which is expected given their increased mass which implies higher potential and kinetic energies (Appendix A.1(c)). The rotation and translation velocities of the SP2B blocks are also higher, suggesting that the larger blocks are globally the least slowed down by their interactions with the terrain. The maximum passage velocity of the SP2B block through the EC11 barrier is 9.92 m/s compared to 6.18 m/s for the SP2A block. Similar remarks can be drawn for the maximum passage velocities through the EC12 barrier (Appendix A.2(c)): the maximum passage velocity of the SP2B blocks is 19.34 m/s compared to 18.93 m/s for the SP2A blocks. For profile P2, the trend observed in terms of increasing translation and rotation velocities and energies is the opposite of that found for profile P1. Indeed, we notice a slight decrease in the translation and rotation velocities of the blocks SP2B with respect to the blocks SP2A (Appendices A.3(b), A.3(b), A.3(c), and A.4(c)). This effect is related to the passage of the blocks on the gravel slope where they tend to roll and slow down. The average rotation velocity of the blocks (0.87 rps) is twice as fast when passing the EC22 than when passing the EC21 (0.59 rps). At the passage of the barriers EC21 and EC22, the total average energies of the blocks are almost unchanged (42.99 kJ for the barrier EC21 against 41.8 kJ for the barrier EC22) with a modification of the mode of energy transfer: the blocks move with a translation energy of 40.4 kJ and a rotational energy of 2.59 kJ at the EC21 barrier, versus 36.37 kJ in translation and 5.43 kJ in rotation at EC22, respectively.

5.4. Small elongated block (SP3A)

It is recalled here that block SP3A is the only virtual block whose geometry is that of a boulder launched during the experimental campaign (block number 89) for profile P2. It was located and photographed on the intermediate track of profile P2 after the test and then

reconstructed by photogrammetry. Although it was used exclusively in profile P2, we wanted to use it also in profile P1 (in simulations) because of its elongated shape. This allowed us to carry out a complete study on the effect of shape for both profiles. Although the initial release condition of the block could not be identified (orientation and position), this block is the only objective point of comparison between the simulations and the field observations.

For profile P1, no trajectory reaches the first EC11 barrier (Fig. 11); only one block approaches it without crossing it. For this profile, there are two preferential deposition zones and two types of associated behavior. The first zone is located right before the slope at $X = 5$ m (close to the launching position), where the block immediately “sinks” into the ground and slides a little, then stops very early at the top of the slope. The second zone is located around the distance $X = 18$ m. The maximum distance reached by one of the blocks is 24 m which corresponds to a position near the EC11 barrier. For profile P2, about 15 blocks stop before the first gravel slope. Some blocks deviate towards profile P1 (*i.e.*, to the left) and get stuck at the top of the rock-cut. These observations coincide with field observations which show that all the boulders remaining at the top of the slope are classified as elongated boulders. The preferred deposition zone for SP3A blocks is between 40 m and 45 m for profile P2. The maximum distance reached by one of these blocks is 68 m. It should also be underlined that the stop position of the block 89 (released during the experimental tests) is included in this preferential zone corresponding to the most frequent deposition runout distance (see Fig. 11, star symbol).

5.5. Influence of block size on the runout distances

Since the experimental distribution of block shapes is not uniform and the numerical block shapes are not representative of all blocks thrown, direct comparison between the experimental and numerical data is not trivial. One of the main practical questions is whether the final propagation distances of the heavier blocks is longer than that of the blocks considered lighter in this dataset. To answer this question we plotted in Fig. 12(a) the experimental stop positions of the blocks as a

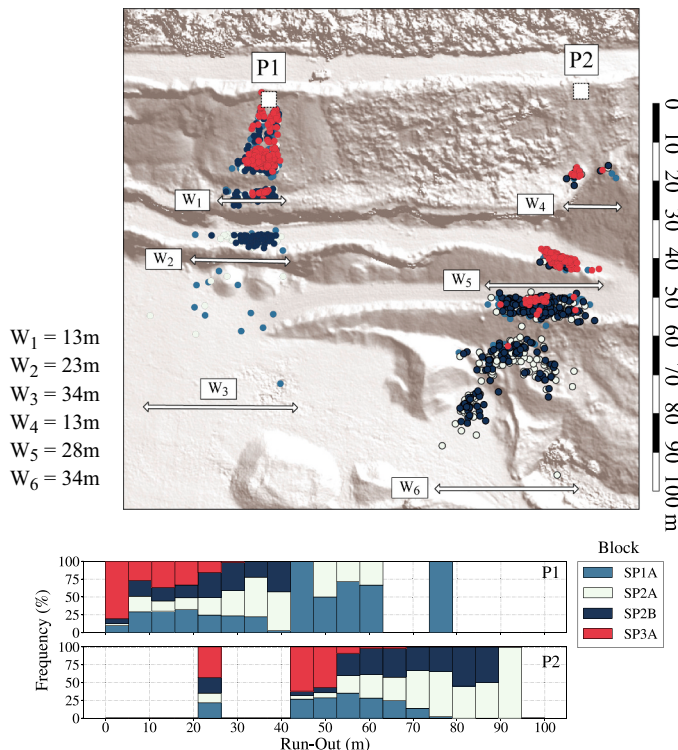


Fig. 13. Simulations: (a) stop positions for each shape, classified by elongation (s_c), and (b) histograms – for profiles P1 and P2 – showing the frequency of the deposition according to the shape over the runout axis. The shape SP3A is the only “elongated” one – all the others are classified as “compact” shapes.

function of their mass; Fig. 12(b) shows, for each group of block (according to their associated color), the probability of stop position as a function of their runout distances.

When analysing Fig. 12, it might be noticed that the larger the blocks, the greater the distances traveled. However, this statement made in reverse cannot be established: some blocks with a mass between 400 kg and 800 kg also end at great distances; as well as a block shortly after the barrier EC12 (profile P1) that has a mass between 200 kg and 400 kg.

For comparison, Fig. 13 summarises the main simulation results of shape and size effects on the runout distances, passing probabilities through all virtual barriers, and spatial distribution in the deposition zones. Within profile P1, we see in Fig. 13(b) a higher density of stop positions in the area located before the EC11 barrier. Concerning blocks SP2A and SP2B (which both have the same shape but different volumes), we notice that the heavier blocks (thus with shape SP2B) have a higher probability to go further than the lighter ones (with shape SP2A).

To illustrate this point, between the runout distances of 50 m and 70 m, no SP2B block reaches the tie of the slope whereas 20% of the blocks of shape SP1B does. All other stopping points being equally distributed, one might say that, given their volumes, the heavier blocks are the ones that cover longer distances. It should be noted that the influence of block size is rather limited here by the fact that the blocks in our tests have sizes and weights of the same order. Further experiments with larger (and smaller) masses may reveal more insights. Anyway, one may ask whether this is a mass effect or rather a geometric effect. In an attempt to answer this question, we wanted to find the link between the elongation coefficient s_c and the distance covered.

5.6. Influence of the block shape on the runout distances

For a better understanding of the role of block shape on the runout distances, we studied how the blocks were distributed in deposits A and B of the profiles P1 and P2 (Fig. 9) according to their shape (Table 7). In

Table 7

Spatial distribution of experimental stop positions in deposits A and B of the profiles P1 and P2 (see Fig. 9) according to their elongation coefficient (s_c).

Deposit A		Deposit B		
Compact	Elongated	Compact	Elongated	
1	0.00%	2.44%	0.00%	8.51%
2	0.00%	2.44%	0.00%	6.38%
3	21.95%	26.83%	31.91%	34.04%
4	34.15%	12.20%	17.02%	2.13%

Table 8

Spatial distribution of the simulated stop positions according to the block elongations (s_c) within both profiles.

Deposit A		Deposit B		
Compact	Elongated	Compact	Elongated	
1	51.95%	94.92%	2.73%	6.25%
2	24.74%	5.08%	17.06%	82.81%
3	20.96%	0.0%	46.61%	10.55%
4	2.34%	0.0%	33.59%	0.39%

addition, the main simulation results dealing with the shape effect on the runout distance are presented in Fig. 13 and summarised in Tables 8 and 9. From an experimental point of view, we notice that, for the deposits A1, A2, B1, and B2, the blocks are exclusively of elongated shape (Table 7), which confirms the previous observations. For deposit area A3, there is a rather balanced distribution between compact and elongated shapes (9 compacts, 11 elongates). In the deposit area A4, the blocks are no longer evenly distributed: 34.15% (14) of compact blocks lie in this zone, against only 12.2% (5) of elongated one. In other words, a block at the tie of profile P1 is 3 times more likely to be compact than elongated. For the B3 deposit (profile P2), we observe that compact and elongated shapes are almost equally distributed: 31.91% versus 34.04%, respectively. In contrast, as soon as the blocks pass over the second track, only 11% of the blocks that settle in the B4 area are elongated, as opposed to 89% that are compact, which confirms the preponderance of “homogeneously shaped” blocks (in view of the angular distribution of surface-to-centre distances) for covering long distances.

From a numerical point of view, it is clear that the compact shaped blocks propagate over longer distances than the elongated shaped blocks (Table 8). For the elongated block shape SP3A, more than 95% of the blocks remain at the top of the slope, including 5% that approach the EC11 barrier – hence a very marked effect of shape. The SP1A blocks (compact shape but with of smaller volume than SP3A blocks that are 1.5 times bigger in volume) are distributed on the slope in a similar way to the SP3A blocks: 92.5% of these blocks remain at the top of the slope. However, none of the SP3A blocks passed through EC11 and EC12 barriers (Table 8), whereas 4.7% of the SP1A blocks did. There appears to be, for profile P1, an effect related to the size of the block, but it is the shape effect that seems to be predominant on the runout distance.

The preferential block deposition zone for profile P2 is located beyond the second barrier: less than 20% of the blocks remain on the slope. Among these blocks, 82.81% are classified as elongated, against only 17.06% of compact blocks. The probability to find an elongated block on the very bottom of the quarry deposition zone is 2% (0.39% of the elongated blocks), against 98% chance to find a compact block. For the volume of the blocks, the observed differences (blocks SP2A and SP2B) are not significant considering the particular behavior of the blocks on the gravel slope (mainly rolling with almost no bounce). The shape of the blocks has in this case the predominant effect given the particular topography of profile P2 (see Fig. 14).

Table 9

Virtual barrier crossing-rates of the numerical blocks by the virtual barriers according to their shape.

	Compact	Elongated
EC11	■ 48.02%	□ 5.08%
EC12	■ 2.34%	□ 0.0%
EC21	■ 98.26%	■ 99.21%
EC22	■ 97.26%	■ 93.75%

5.7. Influence of the block shape on the lateral deviation

The lateral deviation of a block can be characterised by the width W in the direction perpendicular to the direction X of descent, relative to the stop position L along the X axis for each studied profile (Fig. 15). Note that the X direction is taken here roughly as the downward vertical axis in the figure. This ratio W/L can also be related to a lateral dispersion angle $\alpha = \tan^{-1}(W/L)$: a negative angle indicates that the block deviates toward its left (to the right from the reader's perception of the figures seen from above), and a positive angle corresponds to a deviation to the right.

Concerning the results relating to lateral deviation, the values obtained from all the simulations performed (for the four block geometries, Fig. 13) coincide quite well with those of the experimental results (Fig. 9). The maximum spread observed in experiments at the bottom of the slope is 26.3 m for profile P1, and 51.4 m for profile P2. In simulations, these values are higher for profile P1 (33.6 m) and lower for profile P2 (34 m), i.e., a difference of respectively 21.7% and 33.8%, which is still acceptable. It is possible to determine, based on the simulated trajectories, the widths of the barriers (W_1 to W_6) to be

implemented in the context of a structural design (EC11: 12.7 m, EC12: 22.6 m, EC21: 12.75 m, and EC22: 27.5 m). On the opposite, the experimental dataset is limited to the stop positions and not to the whole trajectories, making it impossible to determine the good lateral dispersion of the blocks at virtual barriers vicinity.

Table 10 presents, for each block shape and profile, the experimental and numerical deviation angles. These values correspond to the maximum opening, α_{P1}^{\max} and α_{P2}^{\max} , of the "cone" delimiting the spread of deposits for the profiles P1 and P2, respectively. It can be noted that the angles of deviation from the reference axis seem to be related to the topography of the terrain and also to the geometry of the blocks. For the compact blocks (SP1A, SP2A, and SP2B), the average deviation from the reference axis are $\langle \alpha_{P1} \rangle = +5.72^\circ$ and $\langle \alpha_{P2} \rangle = +10.55^\circ$. Block SP3A, with its elongated shape, tends to deviate slightly less on average than the other block shapes: $\langle \alpha_{P1} \rangle = +4.81^\circ$ and $\langle \alpha_{P2} \rangle = +7.88^\circ$. The block

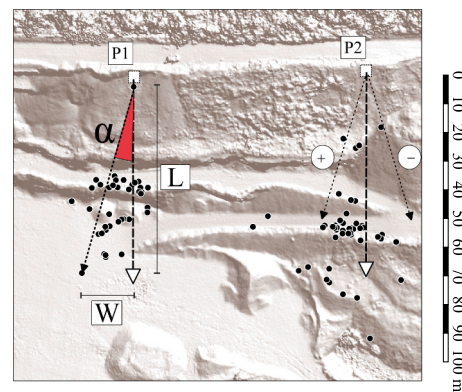


Fig. 15. Lateral dispersion conventions.

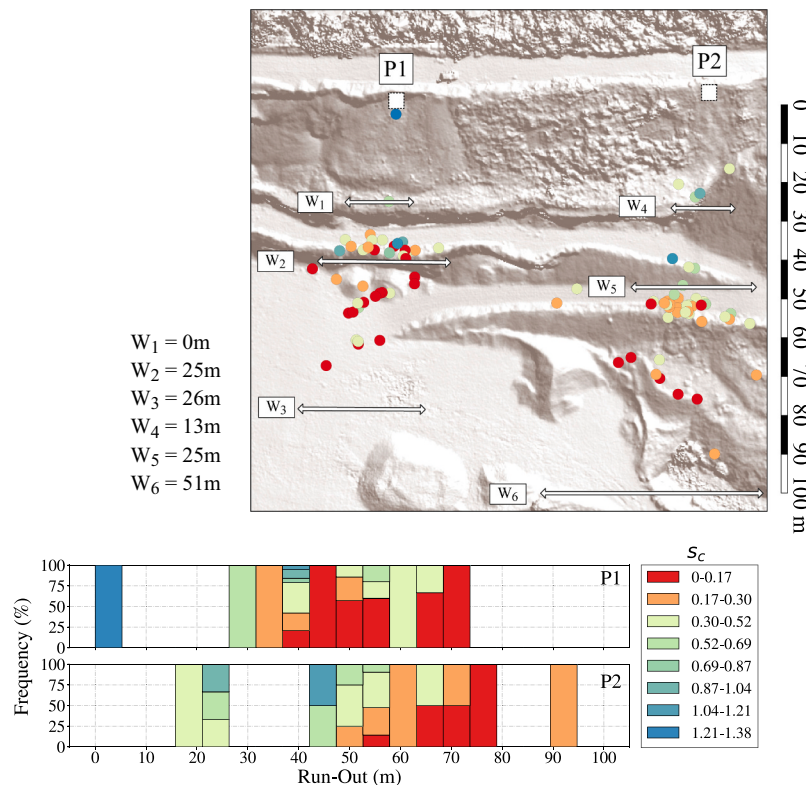


Fig. 14. Experimental results: (a) stop positions according to the shape elongation coefficient s_c . Blocks having low s_c go further. (b) Histogram showing the frequency of deposition of each block according to their shape over the runout axis – for both profiles P1 and P2. Compact blocks can be easily distinguished by warm colors and elongated ones by cold colors.

Table 10

Average value for deviation angle for simulations compared to experimental results.

	$\langle \alpha_{P1} \rangle$	$\langle \alpha_{P2} \rangle$
SP1A	+5.25	+10.49
SP2A	+5.21	+12.26
SP2B	+7.62	+11.59
SP3A	+4.81	+7.88
Field observation	+5.09	+6.62

geometry thus plays a crucial role in its lateral deviation, as it was previously the case for the propagation distances. In profile P1, we notice that the larger the block, the more it tends to deviate laterally, which is less obvious for profile P2. These results are in agreement with the experimental observations.

6. Discussion and conclusions

The good agreement between the numerical results and those obtained in the framework of the C2ROP experimental campaign, demonstrates the ability of the proposed deterministic code to produce relevant insights on the propagation path, the kinematics and the final deposits of boulders propagating along a steep slope. For example, it has been shown that virtual barrier crossing velocities are in accordance with those of numerous experimental records. Moreover, stopping zones are in close agreement with the field observations.

The strength of the proposed procedure is to take into account the actual geometry of the rocks and the complexity of the surface topography. For sake of efficiency and simplicity, a limited number of geometries were considered in this study. Improvements of the numerical model are nevertheless possible, it would be advisable, for example, to optimize the precision of the triangular mesh necessary to limit the inaccuracies due to the roughness and the resolution of the terrain model or to take into account the various volumes and shapes of blocks.

The computation model is also based on a limited numbers of physical parameters that can be defined by simple launch tests in the field. Each set of parameters is set as a function of the nature of the soil, regardless the size or shape of the blocks as their geometry does not varied that significantly in the experiment. The collision law is minimalist but guarantee a well-controlled energy ratio at each hit of the soil. Three soil types were considered, which in retrospect is sufficient to describe the complexity of the experimental site.

The approach offers the ability to establish a statistically predicted deposition zone for each block according to its geometry, mass, and the launching conditions. For each digital block tested, the deposition zone is very extensive, which demonstrates the importance of block shape and terrain topography on the trajectory and the propagation distance of the blocks.

In experiments, each block was released only once, which regrettably greatly limits the interpretation of the results obtained. Even if the simulations do not reproduce faithfully the whole set of experimental observations, the trajectories obtained may correspond to events that have not yet occurred. For the numerical trajectories obtained with block SP3A, for example, we have several possibilities of stop positions, whereas the real block 89 (with shape SP3A) was only launched once. However, the deposition zone of the numerical blocks seems to enclose quite tightly the experimental zone, with a satisfactory accuracy.

Given the rather significant time required for each series of DEM simulations, the analysis focused on four arbitrary block geometries (three compact shapes and one elongated shape). This was followed by 256 simulations for a single elongated block, while having 3 times more results for compact shapes. This choice is not representative of the real distribution of the blocks but it provides relevant hints about the influence of block shape on the runout distance or on the propagation path of the blocks. A weighted balance that relates block size and shape could improve the quality and accuracy of the results that have been produced,

especially for the calculation of the probabilities of barrier crossing velocities and for the estimation of the final depositions. However, as the shape and mass properties were not evenly distributed, our conclusions remain quite satisfactory, although incomplete.

The sensitivity of block shape on propagation distances and energy dissipation appears to be meaningful, as does the size of the blocks. Likewise, the initial launching conditions (including initial orientation of the boulders) has a strong influence on the block propagation. This was particularly noticed when analyzing preferential deposition zones. But still, depending only on the elongation coefficient s_c (and despite the boulder mass), the runout distance is globally reduced for elongated blocks. From the results obtained it is clear that compact shaped blocks propagate over longer distances than elongated blocks. Size effects on the runout distance were also noticed but it is the shape effect that seems to be predominant. As it was experimentally and numerically found, the shape of the boulders has also a great influence on their lateral deviation; this aspect is often less exploited since most codes do not take into account, explicitly, the shape of the blocks. In particular, it was demonstrated that elongated shapes tend to deviate slightly less on average than the other blocks shapes. Conversely, the larger the block, the more likely it is to deviate laterally.

A limitation of the numerical model, for comparison with the experimental results is directly related to the fact that soil deformation is not directly taken into account considering successive impacts. In terms of energy dissipation, the changes undergone by the impacted soil during the execution of the experimental tests would have deserved to be taken into account in the simulations. This would have made it possible to integrate the change in the energy absorption/restitution capacity of the soil, in particular for the first impacts close to the launching area. This change can be achieved through soil hardening (irreversible deformations), or even by changing the profile if one of the blocks were to remain in place; this would critically alter the topography and prevent the passage of a new block through this area (which did happen in the experimental tests). This is not currently integrated into the presented model, and it is possible that the results obtained for the passing probabilities may diverge from numerical results simply because the local geometric parameters (and why not the dissipation parameters) should have been updated after each first impact. Other changes in the field are to be mentioned: the blocks that were deposited in the intermediate track of profile P1 (deposit 3A) were not removed. Thus, some blocks remained stuck in this part of the profile because of the blocks that were already there. The same remark can be made for the blocks deposited at the bottom of the slope. This problem has less incidence for profile P2. In addition, five blocks have broken along the path. For the sake of simplicity, we have removed the multiple stopping points related to these tests from our analysis.

In fact, the use of deterministic codes is not comfortable for an operator who would be in charge of forecasting the hazards of a threatening event. He would be faced with a delicate and uncertain choice of which parameters to use. A good physics background and a significant expertise in the field of rockfall is generally enough; but it is also up to each operator to establish his own database. It is important to remember that when considering many configurations, whether on a large scale or not, the parameter optimization exercise becomes essential. Following a rigorous methodology during the parameter calibration process allows, over time, to refine the expertise and leads to better predictions.

From the obtained results, a good knowledge of the physical mechanisms involved in the energy dissipation process of boulder falls, for the use of trajectory analysis codes, seems important. But it is not necessarily essential given the large variability introduced by the shape of the block and the realistic topography. For engineering practice, the use of 3D simulations can lead advantageously to a first estimation of the most likely propagation corridors. We advise engineers to link field observations to the results of numerical simulations to improve their expertise.

Funding

This work was supported by the French company IMSRN (www.imsrn.com) and the French National Association for Research and Technology (ANRT) [CIFRE Grant No. 2016/0134].

CRediT authorship contribution statement

B. Garcia: Conceptualization, Methodology, Formal-analysis, Investigation, Resources, Data-curation, Writing-original-draft, Writing-review-editing, Visualization. **P. Villard:** Conceptualization, Methodology, Software, Formal-analysis, Investigation, Resources, Writing-original-draft, Writing-review-editing, Supervision, Project-administration, Funding-acquisition. **V. Richefeu:** Conceptualization, Methodology, Software, Formal-analysis, Investigation, Resources, Writing-original-draft, Writing-review-editing, Supervision, Project-administration, Funding-acquisition. **D. Daudon:** Conceptualization, Methodology, Formal-analysis, Investigation, Writing-original-draft, Writing-review-editing, Supervision, Project-administration, Funding-

acquisition.

Declaration of Competing Interest

The authors declare that they have no known competing financial interests or personal relationships that could have appeared to influence the work reported in this paper.

Data availability

The data will be soon made available to the community. With such data, different scientific teams would be able to benchmark (or simply test) their own rockfall models.

Acknowledgments

Authors thank F. Bourrier and D. Toe for sharing experimental data used in this work.

Appendix A. Simulation results – zoning (c)

A.1. Barrier EC11

Table A.1

	Average	Std. Deviation	95% P	Median	Max
(a) Block SP1A/ EC11/ Profil P1					
Passing height (m)	0.75	0.15	0.96	0.76	1.00
Velocity (m/s)	2.64	1.24	4.68	2.80	5.12
Translation energy (kJ)	1.46	1.18	3.78	1.34	4.51
Rotation energy (kJ)	0.11	0.13	0.38	0.06	0.43
Rotation velocity (rps)	0.42	0.20	0.74	0.45	0.82
Total energy (kJ)	1.57	1.26	3.98	1.41	4.76
(b) Block SP2A/ EC11/ Profil P1					
Passing height (m)	0.51	0.16	0.75	0.51	0.84
Velocity (m/s)	3.62	1.35	5.57	3.69	6.18
Translation energy (kJ)	10.97	6.94	22.85	10.03	28.14
Rotation energy (kJ)	1.44	1.00	3.29	1.46	3.85
Rotation velocity (rps)	0.58	0.21	0.89	0.59	0.98
Total energy (kJ)	12.40	7.68	25.68	12.03	30.32
(c) Block SP2B/ EC11/ Profil P1					
Passing height (m)	0.07	0.12	0.27	0.07	0.42
Velocity (m/s)	4.54	1.66	7.39	4.59	9.92
Translation energy (kJ)	20.66	13.96	48.25	18.60	86.95
Rotation energy (kJ)	2.16	1.84	5.50	1.94	11.92
Rotation velocity (rps)	0.72	0.26	1.18	0.73	1.58
Total energy (kJ)	22.82	15.25	52.17	20.58	96.20
(d) Block SP3A/ EC11/ Profil P1					
Passing height (m)					0.84
Velocity (m/s)					2.92
Translation energy (kJ)					2.19
Rotation energy (kJ)					0.00
Rotation velocity (rps)					0.46
Total energy (kJ)					2.19

Single value

A.2. Barrier EC12

Table A.2

	Average	Std. Deviation	95% P	Median	Max
(a) Block SP1A/ EC12/ Profil P1					
Passing height (m)	0.54	0.19	0.83	0.56	0.83
Velocity (m/s)	5.26	1.10	7.37	5.48	7.59
Translation energy (kJ)	4.95	2.04	9.39	5.16	9.90
Rotation energy (kJ)	1.59	0.96	3.60	1.47	3.80
Rotation velocity (rps)	0.84	0.18	1.17	0.87	1.21
Total energy (kJ)	6.54	2.87	12.95	6.08	13.70
(b) Block SP2A/ EC12/ Profil P1					
Passing height (m)	1.65	1.52	5.08	1.17	5.82
Velocity (m/s)	12.55	6.80	18.78	16.48	18.93
Translation energy (kJ)	149.35	104.98	260.15	200.29	264.18
Rotation energy (kJ)	3.91	3.91	11.91	2.63	19.42
Rotation velocity (rps)	2.00	1.08	2.99	2.62	3.01
Total energy (kJ)	153.26	103.79	262.50 ¹	203.30	266.49
(c) Block SP2B/ EC12/ Profil P1					
Passing height (m)	2.49	2.10	5.94	1.53	10.48
Velocity (m/s)	11.87	6.23	18.65	14.35	19.34
Translation energy (kJ)	158.33	120.65	307.51	181.95	330.64
Rotation energy (kJ)	5.30	4.16	14.63	4.29	22.73
Rotation velocity (rps)	1.89	0.99	2.97	2.28	3.08
Total energy (kJ)	163.63	119.44	309.45	193.81	333.13

A.3. Barrier EC21

Table A.3

	Average	Std. Deviation	95% P	Median	Max
(a) Block SP1A/ EC21/ Profil P2					
Passing height (m)	0.67	0.38	1.48	0.55	1.93
Velocity (m/s)	6.41	1.31	8.48	6.47	9.60
Translation energy (kJ)	7.35	2.89	12.36	7.19	15.85
Rotation energy (kJ)	0.22	0.31	0.88	0.06	1.51
Rotation velocity (rps)	0.59	0.56	1.65	0.42	2.16
Total energy (kJ)	7.56	3.01	12.91	7.36	16.51
(b) Block SP2A/ EC21/ Profil P2					
Passing height (m)	1.03	0.44	1.98	0.87	2.29
Velocity (m/s)	6.74	1.44	9.08	6.75	11.07
Translation energy (kJ)	35.04	14.30	60.86	33.56	90.28
Rotation energy (kJ)	2.40	2.25	6.99	1.95	9.82
Rotation velocity (rps)	0.69	0.43	1.39	0.73	1.65
Total energy (kJ)	37.44	15.74	66.55	35.75	97.04
(c) Block SP2B/ EC21/ Profil P2					
Passing height (m)	1.10	0.46	2.05	0.96	2.61
Velocity (m/s)	6.60	1.49	8.76	6.71	10.01
Translation energy (kJ)	40.40	17.05	67.86	39.77	88.49
Rotation energy (kJ)	2.59	2.78	8.56	1.84	12.76
Rotation velocity (rps)	0.59	0.42	1.31	0.61	1.60
Total energy (kJ)	42.99	18.98	75.23	41.21	95.17
(d) Block SP3A/ EC21/ Profil P2					
Passing height (m)	0.61	0.45	1.66	0.43	2.02
Velocity (m/s)	5.44	1.15	7.19	5.36	8.82
Translation energy (kJ)	7.94	3.35	13.30	7.39	20.02
Rotation energy (kJ)	0.13	0.40	0.97	0.01	2.97
Rotation velocity (rps)	0.87	0.18	1.14	0.85	1.40
Total energy (kJ)	8.07	3.49	13.69	7.47	21.15

A.4. Barrier EC22

Table A.4

	Average	Std. Deviation	95% P	Median	Max
(a) Block SP1A/ EC22/ Profil P2					
Passing height (m)	0.61	0.38	1.20	0.59	1.57
Velocity (m/s)	4.83	1.74	7.76	4.73	8.66
Translation energy (kJ)	4.52	3.00	10.34	3.85	12.88
Rotation energy (kJ)	0.56	0.66	2.03	0.28	2.97
Rotation velocity (rps)	0.88	0.62	2.21	0.81	2.64
Total energy (kJ)	5.09	3.47	11.88	4.24	15.85
(b) Block SP2A/ EC22/ Profil P2					
Passing height (m)	1.30	0.40	1.85	1.31	3.08
Velocity (m/s)	6.27	1.94	9.21	6.48	11.10
Translation energy (kJ)	31.70	17.39	62.59	30.97	90.89
Rotation energy (kJ)	5.41	4.71	14.60	4.27	18.38
Rotation velocity (rps)	1.10	0.63	2.04	1.10	3.04
Total energy (kJ)	37.11	21.22	76.50	35.19	96.97
(c) Block SP2B/ EC22/ Profil P2					
Passing height (m)	1.25	0.41	1.88	1.21	2.09
Velocity (m/s)	6.07	2.09	9.52	6.23	11.53
Translation energy (kJ)	36.37	22.35	80.04	34.29	117.59
Rotation energy (kJ)	5.43	5.23	15.32	4.00	20.72
Rotation velocity (rps)	0.87	0.55	1.71	0.86	2.02
Total energy (kJ)	41.80	26.92	92.78	36.71	137.74
(d) Block SP3A/ EC22/ Profil P2					
Passing height (m)	0.21	0.20	0.69	0.15	1.25
Velocity (m/s)	3.16	1.18	5.49	2.98	7.71
Translation energy (kJ)	2.92	2.32	7.74	2.28	15.27
Rotation energy (kJ)	0.17	0.32	0.87	0.03	2.24
Rotation velocity (rps)	0.93	0.47	1.82	0.85	2.32
Total energy (kJ)	3.09	2.47	7.84	2.32	17.50

References

- Bar, N., Nicoll, S., Pothitos, F., 2016. Rock fall trajectory field testing, model simulations and considerations for steep slope design in hard rock. In: Proceedings of the First Asia Pacific Slope Stability in Mining Conference, pp. 457–466.
- Bartelt, P., Caviezel, A., Christen, M., Lu, G., Gerber, W., Buhler, Y., 2018. On four frictional mechanisms in rockfall analysis: ground deformation, surface roughness, vegetation drag and basal sliding with rebound. In: Colloque International RSS - Rock Slope Stability 2018. WSL Institute of Snow and Avalanche Research SLF, Switzerland.
- Bourrier, F., Acary, V., 2022. Predictive capabilities of 2d and 3d block propagation models integrating block shape assessed from field experiments. *Rock Mech. Rock Eng.* 55 (2), 591–609.
- Bourrier, F., Berger, F., Tardif, P., Dorren, L., Hungr, O., 2012. Rockfall rebound: comparison of detailed field experiments and alternative modelling approaches. *Earth Surf. Proc. Land.* 37 (6), 656–665.
- Bourrier, F., Toe, D., Garcia, B., Baroth, J., Lambert, S., 2020. Experimental investigations on complex block propagation for the assessment of propagation models quality. *Landslides*.
- Cottaz, Y., Barnichon, J.-D., Badertscher, N., Gainon, F., 2010. Pir3d, an effective and user-friendly 3d rockfall simulation software: formulation and case-study application.
- Coumans, E., Bai, Y., 2016–2021. Pybullet, a python module for physics simulation for games, robotics and machine learning. <http://pybullet.org>.
- Cundall, P.A., Strack, O.D.L., 1979. A discrete numerical model for granular assemblies. *Geotechnique* 29, 47–65.
- Dorren, L., 2016. Rockyfor3d (v5.2) revealed – transparent description of the complete 3d rockfall model.
- Dorren, L., Berger, F., Putters, U.S., 2006. Real-size experiments and 3-d simulation of rockfall on forested and non-forested slopes. *Nat. Hazards Earth Syst. Sci.* 6 (1), 145–153.
- Erdogan, S., Quiroga, P., Fowler, D., Saleh, H., Livingston, R., Garboczi, E., Ketcham, P., Hagedorn, J., Satterfield, S., 2006. Three-dimensional shape analysis of coarse aggregates: New techniques for and preliminary results on several different coarse aggregates and reference rocks. *Cem. Concr. Res.* 36 (9), 1619–1627.
- Garcia, B., 2019. Analyses of the mechanical interaction between a rock mass and a slope: engineering applications. Thèse, Université Grenoble Alpes. Doctorat dirigé par Villard, P., Richefeu, V. et Daudon, D. Matériaux, Mécanique, Génie civil, Electrochimie. Université Grenoble Alpes 2019.
- Garcia, B., Villard, P., Richefeu, V., Daudon, D., 2017. Experimental and dem analysis of the dissipation involved in the collision of a boulder with a substratum. *EPJ Web Conf.* 140, 16010.
- Heim, A., 1932. Bergsturz und menschenleben. zürich, fretz und wasmuth. In: *Vierteljahrsschrift der Naturforschenden Gesellschaft in Zürich*, pp. 77.
- Hungr, O., Evans, S., 1988. Engineering evaluation of fragmental rockfall hazards. In: *Proceedings of the 5th Int. Symposium on Landslides*, Lausanne, pp. 685–690.
- Jaboyedoff, M., Labiouse, V., 2011. Technical note: preliminary estimation of rockfall runout zones. *Nat. Hazards Earth Syst. Sci.* 11 (3), 819–828.
- Kobal, M., Zabota, B., 2018. State of the art on rockfall modelling: report on the state of the art of rockfall modelling in the alps. RocktheAlps – Interreg Alpine Space.
- Kozicki, J., Donze, F., 2008. Yade-open dem: an opensource software using a discrete element method to simulate granular material. *Eng. Comput.* 26.
- Leine, R.I., Schweizer, A., Christen, M., Glover, J., Bartelt, P., Gerber, W., 2014. Simulation of rockfall trajectories with consideration of rock shape. *Multibody Sys. Dyn.* 32 (2), 241–271.
- Pichler, B., Hellmich, C., Mang, H.A., 2005. Impact of rocks onto gravel design and evaluation of experiments. *Int. J. Impact Eng.* 31, 559–578.
- Richefeu, V., Villard, P., 2016. Modeling Gravity Hazards from Rockfalls to Landslides. ISTE Press Ltd., Elsevier Ltd., UK.
- Rochet, L., 1987. Application des modèles numériques de propagation à l'étude des éboulements rocheux. *Bulletin de liaison des Laboratoires des Ponts et Chaussées, Risques Naturels* (150/151), 84–95.
- Sneed, E.D., Folk, R.L., 1958. Pebbles in the Lower Colorado River, Texas: a Study in Particle Morphogenesis. *J. Geol.* 66, 114–150.
- Valagussa, A., Frattini, P., Crosta, G., 2014. Earthquake-induced rockfall hazard zoning. *Eng. Geol.* 182.
- Volkwein, A., Schellenberg, K., Labiouse, V., Agliardi, F., Berger, F., Bourrier, F., Dorren, L.K.A., Gerber, W., Jaboyedoff, M., 2011. Rockfall characterisation and structural protection: a review. *Nat. Hazards Earth Syst. Sci.* 11 (9), 2617–2651.
- Williams, E.M., 1965. A method of indicating pebble shape with one parameter. *J. Sediment. Res.* 35 (4), 993–996.
- Zingg, T., 1935. Beitrag zur schotteranalyse (contribution to gravel analysis). *Schweizerische Mineralogische und Petrographische Mitteilungen - (Swiss Bull. Mineral. Petrol.)* 15, 39–140.